



The Impact of Solar Irradiance on Visible Light Communications

Mohamed Sufyan Islam , *Graduate Student Member, IEEE*, Stefan Videv, Majid Safari, *Member, IEEE*, Enyuan Xie , Jonathan J. D. McKendry, Erdan Gu, Martin D. Dawson, *Fellow, IEEE*, and Harald Haas, *Fellow, IEEE*

Abstract—This paper aims to address the perception that visible light communication (VLC) systems cannot work under the presence of sunlight. A complete framework is presented to evaluate the performance of VLC systems in the presence of solar irradiance at any given location and time. The effect of solar irradiance is investigated in terms of degradations in signal to noise ratio, data rate, and bit error rate. Direct current (DC) optical orthogonal frequency division multiplexing is used with adaptive bit and energy loading to mitigate DC wander interference and low-frequency ambient light noise. It was found that reliable communication can be achieved under the effect of solar irradiance at high-speed data rates. An optical bandpass blue filter is shown to compensate for half of the reduced data rate in the presence of sunlight. This work demonstrates data rates above 1 Gb/s of a VLC link under strong solar illuminance measured at 50350 lux in clear weather conditions.

Index Terms—Light fidelity (LiFi), OFDM, solar irradiance, visible light communication (VLC).

I. INTRODUCTION

TRAFFIC from wireless and mobile devices will account for two-thirds of the total internet traffic by 2020 [1]. The radio frequency (RF) bandwidth is a scarce resource costing above \$1.28m per 1 MHz in the 2.4 GHz frequency band in the UK [2]. Visible light communication (VLC) offers a much larger frequency bandwidth that is unlicensed and safe to use. VLC has the potential to reuse the existing lighting infrastructure based on light emitting diode (LED) for communications purposes [3]. Light fidelity (LiFi) is the network solution for VLC that is proposed to work seamlessly beside other RF access technologies [3]. A record data rate of 7.91 Gb/s was reported

for orthogonal frequency division multiplexing (OFDM)-based VLC using single violet micro-scale GaN led (micro-LED) [4]. Data rates above 100 Gb/s can be achieved when the complete visible spectrum is utilized [5].

The effect of solar irradiance is considered to be one of the main misconceptions surrounding VLC [6]. It is generally assumed that it could halt the operation of the communication system entirely due to interference. However, the effect of solar irradiance is more apparent as a strong shot noise source rather than an interference source as the sunlight intensity does not vary greatly over short periods of time. This allows multicarrier schemes such as OFDM to allocate the symbols over the usable frequency subcarriers of the deployed bandwidth [7].

The effect of solar irradiance on the performance of optical wireless communications (OWC) and VLC has been investigated in a limited number of works in the literature [8]–[12]. A simplified model was adopted in some of these works by approximating the solar irradiance to a black body radiation [8]. Other works adopted a standardized solar irradiance model [13] that is being used as a reference model in the research on solar energy harvesting [9]. However, the location and time of the studied system play important roles in characterizing the solar irradiance effect on VLC system performance. These important parameters were considered using computer simulation in [10]. However, the direct solar irradiance was not used to characterize the system performance. The solar irradiance was assumed to be incident from a window and reflected on multiple walls before it is collected by the photoreceivers. The impact of solar irradiance on the performance of underwater OWC links was investigated for positive-intrinsic-negative (PIN), avalanche photodiode (APD) and photomultiplier tube (PMT) using Monte Carlo simulation in [9]. It was shown that sunlight degrades the system performance at relatively low depths below 80 meters.

The use of optical filters with a light control film to mitigate the effects of sunlight was proposed in [8], [11]. A filter with a light control film called microlouver is used to restrict the field of view (FOV) and to reduce the background light collected at the photoreceiver. However, the light control film can not adapt to the changes of the photoreceiver orientation and location which limits the solution to fixed point-to-point systems. The objective of this paper is to provide a theoretical and experimental characterization of the solar irradiance effect on high-speed OFDM-based VLC systems. The investigation compares the use of a bandpass optical blue filter to the case where

Manuscript received August 31, 2017; revised January 22, 2018; accepted February 25, 2018. Date of publication March 8, 2018; date of current version March 27, 2018. This work was supported by the UK Engineering and Physical Sciences Research Council under Grants EP/K008757/1, EP/K00042X/1, and EP/M506515/1. This paper was presented in part at the IEEE International Symposium on Personal, Indoor and Mobile Radio Communications, Montreal, QC, Canada, October 2017. (Corresponding author: Mohamed Sufyan Islam.)

M. S. Islam, S. Videv, M. Safari, and H. Haas are with the Institute for Digital Communications, Li-Fi R&D Centre, The University of Edinburgh, Edinburgh EH9 3JL, U.K. (e-mail: m.islim@ed.ac.uk; s.videv@ed.ac.uk; m.safari@ed.ac.uk; h.haas@ed.ac.uk).

E. Xie, J. J. D. McKendry, E. Gu, and M. D. Dawson are with the Institute of Photonics, University of Strathclyde, Glasgow G1 1RD, U.K. (e-mail: enyuan.xie@strath.ac.uk; jonathan.mckendry@strath.ac.uk; erdan.gu@strath.ac.uk; m.dawson@strath.ac.uk).

Color versions of one or more of the figures in this paper are available online at <http://ieeexplore.ieee.org>.

Digital Object Identifier 10.1109/JLT.2018.2813396

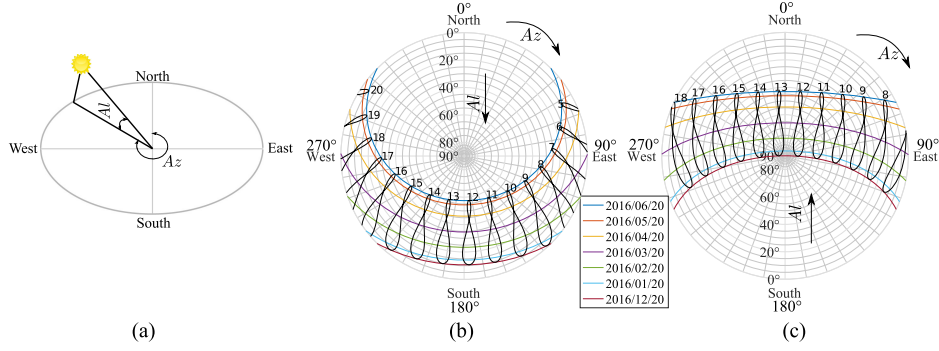


Fig. 1. (a) Solar position described by altitude and azimuth. (b) and (c) Solar position at Edinburgh and Antofagasta, respectively, for each 20th day of each considered month. The time of the day is listed above the elliptical shapes representing the Analemma diagrams.

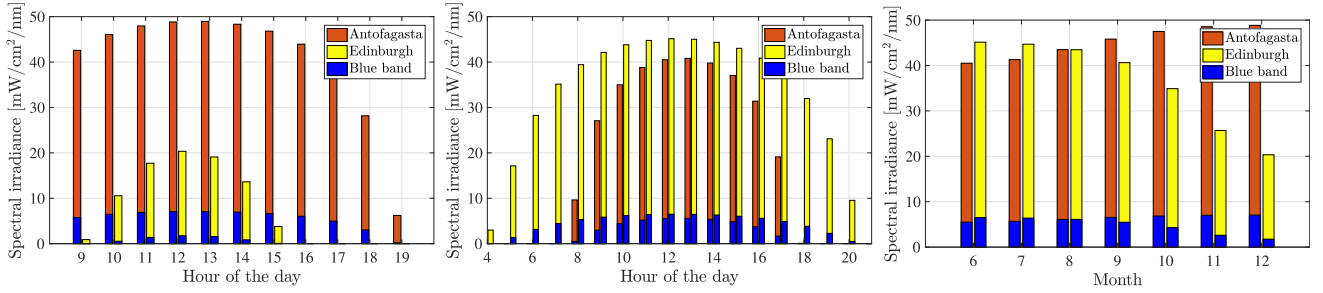


Fig. 2. Total solar irradiance estimated at Antofagasta and Edinburgh on the 20th of December 2016 (left) and on the 20th of June 2016 (center); and at the noon of each 20th day of the second half of the year (right). The blue spectral component of the solar irradiance is shown in blue.

a filter is not considered in front of the photoreceiver. The performance is compared to a benchmark scenario of a dark room where background light does not reach the photoreceiver.

In our previous work [14], we investigated the solar irradiance effect on VLC in Antofagasta, Chile based on worst-case scenarios in terms of location, link orientation and choice of photoreceiver. In this paper, we present a complete framework to investigate the sunlight effect on VLC at any given location and time. The previous literature were mainly based on pulsed modulation techniques [11], [12]. However, an outdoor underwater VLC demonstration achieving a data rate of 58 Mb/s was considered using discrete multi-tone (DMT) [15]. In this work, we demonstrate our results by an experimental proof of concept of a high speed OFDM-based VLC system in Edinburgh, UK achieving data rate above 1 Gbps in the presence of solar irradiance without any optical filtering. The simulation and experimental results show that the solar irradiance affects VLC link performance, but the effects are gradual and depend on a number of other parameters such as link margin. The simulation results show that at least half of the losses in data rate performance can be recovered using an inexpensive commercially available bandpass blue filter.

The rest of this paper is organized as follows. In Section II, we review the solar position and irradiance calculations based on location and time and present the results of two geographical locations. The assumptions of the theoretical study are specified in Section III-A. The signal-to-noise ratio (SNR), the maximum theoretical limit to the data rate and bit error rate (BER) of the system are derived and the system modelling is discussed in Section III-B. An experimental proof-of-concept is presented in

Section IV. The system performance is analyzed and the results are shown in Sections III-C and IV-B. Section V concludes the paper.

II. SOLAR IRRADIANCE AND POSITION

The solar constant flux density P_{SC} is given as 1366.1 W/m^2 outside the Earth's atmosphere by the American society for testing and materials (ASTM) standard (ASTM E-490) [16]. The solar irradiance is not limited to the visible spectrum as it spans the wavelengths from 250 nm to 2500 nm. The solar irradiance at different wavelengths is non-equally attenuated as it travels through the atmosphere due to the different absorption and scattering effects of the air molecules and aerosols. The shortest path for the sunlight exists when the Sun is located at the zenith point (imaginary point above the head of the observer). The optical air mass (AM) is approximated as the ratio of the actual sunlight path to the minimum path at the zenith point. It is given as AM0 for the extraterrestrial irradiance. When the Sun is at angle θ_Z relative to the zenith, the optical AM is approximated as:

$$AM \simeq \frac{1}{\cos \theta_Z}. \quad (1)$$

The solar irradiance at $\theta_Z = 48.2^\circ$ is given at an AM1.5 by the standard (ASTM E-490) [13] as a reference to help the solar energy community in testing and comparing the performance of various solar cells. However, the solar irradiance varies based on the geographical location; seasonal and diurnal variations arising from the rotation of the Earth around the Sun; and the

TABLE I
MODELLING ASSUMPTIONS

Locations	Edinburgh, UK, 55°55'20.4"N 3°10'23.3"W Antofagasta, Ch, 23°27'16.1"S 70°26'21.4"W
Dates	Every 20 th of each considered month
APD model	Hamamatsu S8664-50K
APD detection area, A	19.6 mm ²
Bandwidth, B	60 MHz
APD gain, M	100
Dark current, I_d	3 nA
Blue filter FWHM	50 nm
Maximum transmitted optical power, P_{Max}^L	8 mW
Transmission distance, d	63.85 cm
Half-power semi-angle of the transmitter, $\Phi_{1/2}$	25°

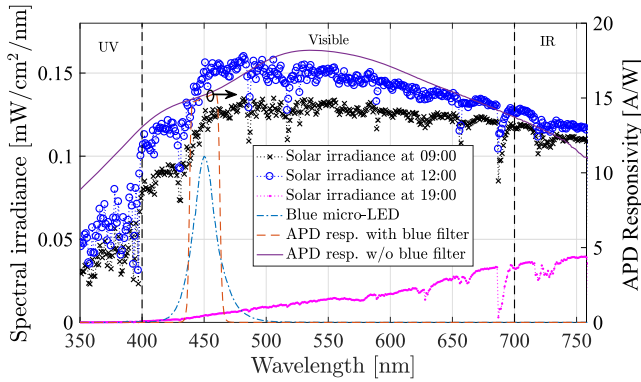


Fig. 3. The predicted solar irradiance in Antofagasta at 9 AM, 12 PM and 19 PM (local time) of the 20th on December 2016 (left), alongside the spectral irradiance of the modeled micro-LED centred at 450 nm (left) and response of the APD with and without considering the transmittance of the blue filter (right).

rotation of the Earth around its own axis. The effect of solar irradiance on VLC varies based on the location and time. Therefore, it is essential to calculate the position of the Sun in the sky in order for the solar irradiance at a particular location and time to be estimated. Various algorithms with different complexities and accuracies for calculating the solar position exist in the astrophysics literature [17]. In Appendix A, we review a simple algorithm based on the ecliptic coordinates with an accuracy of $(1/60)^\circ$ presented in [18] and proposed by the astronomical applications department of the U.S. naval observatory [19].

The horizontal coordinate system is usually used for solar energy applications where the horizon of the observer is considered to be the fundamental plane. The solar position can be described using two angles: altitude Al and azimuth Az . The solar altitude $Al \in [0^\circ, 90^\circ]$ is given as the elevation of the Sun above the horizon. A solar altitude of $Al = 90^\circ$ means that the Sun is at the zenith point. The solar altitude can also be given as $Al = 90^\circ - \theta_Z$. The solar azimuth $Az \in [0^\circ, 360^\circ]$ is given as the angle between the north and the horizontal projection of the line-of-sight (LoS) between the Sun and the observer. Both angles are illustrated in Fig. 1(a) and demonstrated in Fig. 1(b) and (c) for Edinburgh, UK and Antofagasta, Chile on the 20th of each considered month, respectively. The solar altitude is shown to reach the zenith $Al = 90^\circ$ around 13:00 on the 20th of December

2016 for Antofagasta in Fig. 1(c). The time of the day is shown above the analemma diagrams in Fig. 1(b) and (c), which depict the Sun's motion throughout the year when observed at the same location and the same hour of day.

Direct solar irradiance is the sunlight that is directly reaching the surface of the Earth. Global solar irradiance is the combination of the direct and diffused solar irradiance. The simple model of the atmospheric radiative transfer of sunshine (SMARTS) is a transmittance model to evaluate the direct solar irradiance at any particular location and time [20], [21]. The model is used in generating the ASTM standard (ASTM E-490) with a resolution of 0.5–1 nm [16]. The direct solar irradiance is typically stronger than the signal of interest when the total solar irradiance is taken into account. Fortunately, VLC is realized using monochromatic or multi-chromatic optical sources that has fixed and pre-defined spectral irradiance. This allows inexpensive commercially available optical filters to be a practical solution for the degradations caused by solar irradiance. The total predicted solar irradiance is shown in Fig. 2(a) and (b) for Antofagasta and Edinburgh at the noon of December and June solstices, respectively. Monthly comparisons for the total solar irradiance are shown in Fig. 2(c). The total spectral irradiance is calculated for the visible spectrum between 400 nm and 760 nm. The blue component of the solar irradiance for the wavelengths between 425 nm and 475 nm shows the importance of optical filtering in improving the VLC communications performance. Optical filtering is also beneficial for other objectives in VLC. White illumination is generally achieved by coating the blue LED with a yellow phosphor which introduces a slow component into the frequency response of the LED. Blue filters are required to eliminate the slow response component of the yellow phosphor. Monochromatic light sources with narrowband spectral distributions can guarantee a robust VLC system against solar irradiance with the potential of achieving data rates in the orders of multiple Gb/s.

III. THEORETICAL STUDY

A. Modelling Assumptions

An OFDM-based VLC system is assumed due to its robustness against background illumination flickering. The OFDM waveform is required to be both unipolar and real valued. Hermitian symmetry is imposed on the M -ary quadrature amplitude modulation (M -QAM) symbols, to enforce the OFDM time domain signal output into the real domain. This can be written as: $X[k] = X^*[N_{FFT} - k]$, where N_{FFT} is the OFDM frame size. The subcarriers $X[0]$ and $X[N_{FFT}/2]$ are both set to zero. A real-valued OFDM waveform with a direct current (DC) bias is used to modulated the intensity of the LED in what is known as DC-biased optical OFDM (DCO-OFDM). Binary inputs are encoded into multiple M -QAM symbols which are allocated into N_{FFT} subcarriers over a single-sided bandwidth of B . DC bias is used to shift the negative signal samples into positive values. Three scenarios are considered:

- *Dark room (Scenario I)*: assumes an optimal case where no background illumination is reaching the photoreceiver.

This is an ideal scenario as the dominant noise source is the thermal noise.

- *With blue filter (Scenario II)*: assumes that the solar irradiance is collected with a bandpass blue filter in front of the photoreceiver. This is a practical scenario as the useful transmitted signal is passed and any out-of-band signal is filtered. Part of the solar irradiance is passed since it covers a wide wavelength band.
- *Without blue filter (Scenario III)*: assumes a worst case scenario where the solar irradiance is collected without any optical filtering in front of the photoreceiver.

The modeling assumptions are presented in Table I. The system uses a blue micro-LED with a pixel size of $100 \times 100 \mu\text{m}^2$ and a maximum optical power of 8 mW. Due to the reduced emission area of micro-LEDs, the capacitance decreases and current density increases allowing for higher 3-dB bandwidths compared to off-the-shelf LEDs [22]. The transmission distance is specified at $d = 63.85$ cm to match with the distance that we have used to measure the spectral irradiance of the micro-LED. The system performance is also investigated at longer distances up to 3 meters in Section III-C. A focusing aspheric condenser optical lens (Thorlabs, ACL4532U-A) is used at the transmitter side, which allows for a small half-power semi-angle at the transmitter $\Phi_{1/2} = 25^\circ$. An optical bandpass blue filter from Edmund Optics is assumed in Scenario II with a center wavelength of 450 nm, a transmittance higher than 90% and a full width at half maximum (FWHM) of 50 nm. The photoreceiver is an APD (Hamamatsu, S8664-50K) where it is assumed to be aligned with the micro-LED. APDs operate at high reverse bias to create an amplification effect that allows incident photons to create an avalanche of electrons. APDs are more sensitive to background noise compared to other photodiodes. However, APDs are used as a worst case choice in this investigation as they are shot-noise limited [23]. The APD will not always be collecting the solar irradiance due to the orientation of the communication link in practical situations. However, the APD is always assumed to be collecting the sunlight in this investigation.

The locations considered are $55^\circ 55' 20.4''\text{N}$ $3^\circ 10' 23.3''\text{W}$ in Edinburgh, UK and $23^\circ 27' 16.1''\text{S}$ $70^\circ 26' 21.4''\text{W}$ in Antofagasta, Chile. The former location is used to compare with the experimental results and the latter is claimed to have the highest solar radiation on Earth [24]. The model considers two dates: summer solstice and winter solstice where the solar position is calculated and used in SMARTS [20], [21] to estimate the hourly solar irradiance data. The model assumes a clear sky scenario due to the irregular variations in the local weather conditions which influence the solar irradiance. This allows us to consider the maximum possible solar irradiance in a pessimistic approach. As the considered locations lie in the north and south hemispheres, the summer solstice at Edinburgh would be winter solstice at Antofagasta and similarly the opposite is true.

B. System Modeling

The OFDM waveform $x(t)$ is transmitted over the VLC channel $h(t)$, before it is distorted with noise $n(t)$ at the receiver.

The received signal $r(t)$ is then sampled at $1/T$ with an analog-to-digital converter (ADC), where T is the sampling period. Fast Fourier transform (FFT) is then applied on the samples after serial to parallel (S/P) conversion. Assuming that the OFDM frame size is large ($N_{\text{FFT}} > 64$) [25], central limit theorem (CLT) can be applied on the combination of noise generated at the receiver. This can be modeled as zero mean additive white Gaussian noise (AWGN) with variance σ_n^2 . The received OFDM waveform $r(t)$ can be given as:

$$r(t) = h(t) * x(t) + n(t). \quad (2)$$

The average photocurrent generated at the APD due to the average optical power received from sunlight is given as:

$$I_b = A_d \int_{350}^{750} P_D^S(\lambda) R(\lambda) T_{bf}(\lambda) d\lambda, \quad (3)$$

where A_d is the APD detection area, $P_D^S(\lambda)$ is the direct solar irradiance given in $\text{W/m}^2/\text{nm}$, $T_{bf}(\lambda)$ is the transmittance of the bandpass optical blue filter, $R(\lambda)$ is the intrinsic responsivity of the APD given in A/W and λ is the wavelength considered for the visible light spectrum mainly from 350 nm to 750 nm.

Similarly, the average photocurrent generated at the APD due to the average optical power received from the micro-LED is given as:

$$I_x = \frac{(m+1)A_d}{2\pi d^2} \int_{350}^{750} P_T^L(\lambda) R(\lambda) T_{bf}(\lambda) d\lambda, \quad (4)$$

where $m = -1/\log_2(\cos(\Phi_{1/2}))$ is the Lambertian order of the micro-LED; d is the Euclidean distance between the micro-LED and the APD; and $P_T^L(\lambda)$ is the transmitted optical irradiance from the micro-LED, which is given as:

$$P_T^L(\lambda) = P_{\text{Max}}^L \frac{P_{\text{Measured}}^L(\lambda)}{\int_{350}^{750} P_{\text{Measured}}^L(\lambda) d\lambda}, \quad (5)$$

where P_{Max}^L is the maximum transmitted optical power of the micro-LED and $P_{\text{Measured}}^L(\lambda)$ is the measured optical irradiance of the micro-LED given in $\text{W/m}^2/\text{nm}$. This was measured at a distance of $d = 63.85$ cm using a Labsphere spectral irradiance head (E1000).

The random arrival of incident photons results in shot noise which can be modeled by a Poisson distribution. However, when the number of incident photons increases, the shot noise is approximated by a Gaussian distribution [26]. The shot noise variance is given by [27]:

$$\sigma_s^2 = 2qM^2 F(I_b + I_x)B, \quad (6)$$

where M is the average gain of the APD, q is the electron charge, B is the bandwidth of the APD and F is the excess noise given as [28]:

$$F = \kappa M + (2 - 1/M)(1 - \kappa), \quad (7)$$

where κ is the holes/electrons ionization rate. The SNR at sub-carrier k can be given by:

$$\gamma_k = \frac{M^2 I_x^2}{\sigma_n^2 / |H(k)|^2}, \quad (8)$$

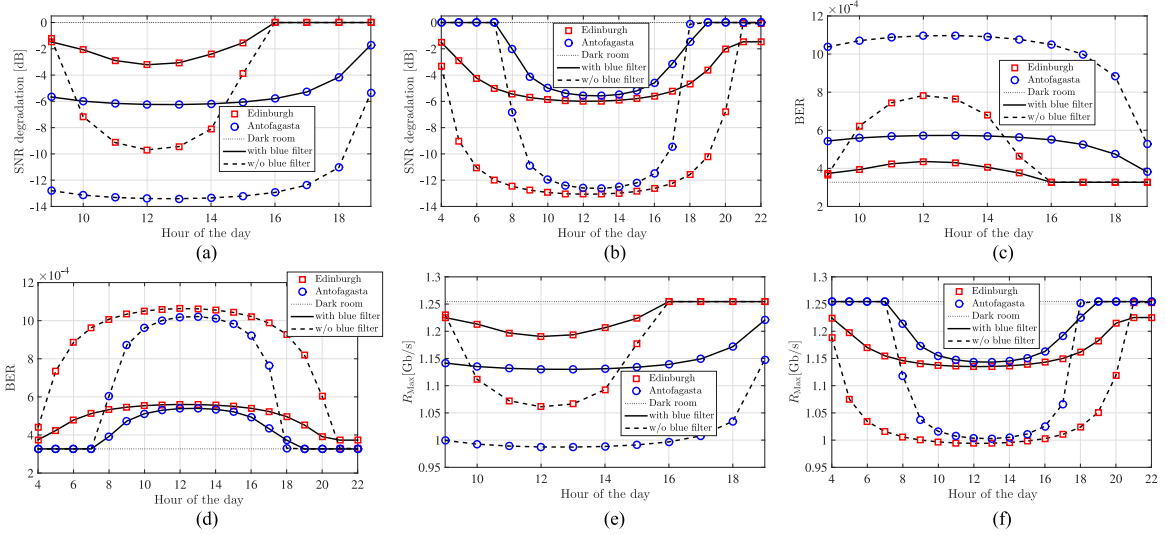


Fig. 4. (a and b) SNR; (c and d) BER; (e and f) maximum theoretical limit to the data rate. All results are presented for the three considered scenarios in Antofagasta and Edinburgh versus time at the 20th of December 2016 (a, c, e) and 20th of June 2016 (b, d, f).

where $H(k)$ is the frequency domain realization of the VLC channel, $\sigma_n^2 = \sigma_s^2 + \sigma_t^2 + \sigma_d^2$ and σ_d^2 is the variance of the dark noise which is given as [27]:

$$\sigma_d^2 = 2qM^2FI_{dg}B + 2qI_{ds}B, \quad (9)$$

where I_{ds} is the surface dark current and I_{dg} is the bulk dark current that experience the avalanche effect of the APD and where $I_d = I_{ds} + MI_{dg}$. The variance of the thermal noise σ_T^2 is given by [29]:

$$\sigma_T^2 = 4 \left(\frac{K_B T}{R_L} \right) F_n B, \quad (10)$$

where K_B is Boltzmann constant, T is the temperature in Kelvin, R_L is the load resistance given as 50Ω and F_n is the photodiode noise figure.

Adaptive bit and energy loading algorithms such as the Levin-Campello algorithm [30] can be used to maximize the data rate by assigning larger constellation sizes on the subcarriers that have higher SNR. The maximum theoretical limit to the data rate of DCO-OFDM can be calculated using the channel capacity defined by Shannon-Hartley theorem [31] when neglecting the DC bias and the optical source nonlinearity [32]. This is given as:

$$R_{\text{Max}} = B \sum_{\substack{k=1 \\ M'_k > 0}}^{N_{\text{FFT}}/2-1} \log_2(1 + \gamma_k), \quad (11)$$

where M'_k is the constellation order of M'_k -QAM used at sub-carrier k .

The system performance in terms of BER can be calculated using the theoretical BER of real-valued OFDM given for frequency selective channels [33]. The BER at subcarrier k can be

given as:

$$\text{BER}(M'_k, \gamma_k) \cong \frac{4}{\log_2(M'_k)} \left(1 - \frac{1}{\sqrt{M'_k}} \right) \times \sum_{l=1}^R Q \left((2l-1) \sqrt{\frac{3\gamma_k}{2(M'_k-1)}} \right), \quad (12)$$

where $Q(\cdot)$ is the complementary cumulative distribution function (CCDF) for the standard normal distribution and $R = \min(2, \sqrt{M'_k})$. The overall system BER can be given as:

$$\text{BER} = \frac{\sum_{\substack{k=1 \\ M'_k > 0}}^{N_{\text{FFT}}/2-1} \text{BER}(M'_k, \gamma_k) \log_2(M'_k)}{\sum_{\substack{k=1 \\ M'_k > 0}}^{N_{\text{FFT}}/2-1} \log_2(M'_k)} \quad (13)$$

C. Results and Discussions

The spectral irradiance of the micro-LED and the amplified responsivity of the APD $MR(\lambda)$ are shown in Fig. 3 with the presence and absence of the optical bandpass blue filter. In addition, the predicted spectral irradiance of the sunlight at Antofagasta is shown at three different times of the summer solstice. It is shown that the solar irradiance is high at the ultra-violet (UV) and blue spectrum bands at sunrise. At sunset it becomes higher at the red and infra-red (IR) spectrum bands. The blue filter captures 70% of the micro-LED irradiance.

The system performance is presented in Fig. 4(a) and (b) as a function of the SNR degradation against the time of the day for both December and June solstice, respectively. The degradation is calculated with reference to the benchmark case of the dark room in Scenario I. It is shown that the SNR degrades by a maximum of -13.4 dB and -9.69 dB at the noon of December solstice in Scenario III at Antofagasta and Edinburgh, respectively. However, when a blue filter is used in front of the

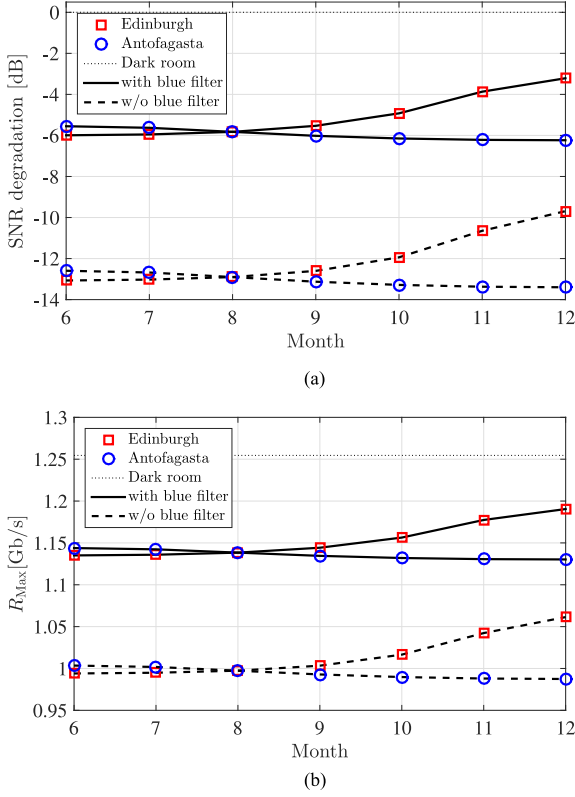


Fig. 5. The system performance presented on monthly basis at the noon of each 20th day of the considered months for the three considered scenarios in Antofagasta and Edinburgh. (a) SNR and (b) Maximum theoretical limit on data rate.

APD, this degradation is reduced to -6.23 dB and -3.214 dB in Scenario II at Antofagasta and Edinburgh, respectively. The high degradation in SNR at Antofagasta is expected due to the higher solar irradiance in December solstice in comparison with Edinburgh as shown in Fig. 2(a). The SNR degradations at Edinburgh for June solstice increase in comparison with December solstice by a maximum increase of 3.38 dB. The SNR degradation is 0.8 dB lower for June solstice compared with December solstice at Antofagasta. A minimum of 6.47 dB improvement in SNR is achieved when blue filters are used in Scenario II. The SNR degradation at Edinburgh are witnessed for longer hours during June solstice due to the longer daylight that is shown in Fig. 1(b). The SNR degradation at Antofagasta and Edinburgh at the 20th day of the noon of the last six months of 2016 is presented in Fig. 5(a). The degradation decreases noticeably as we approach December solstice at Edinburgh, while SNR degradation variations are less noticeable for Antofagasta.

The system performance as a function of the BER against the time of the day is shown in Fig. 4(c) and (d) for 128-QAM DCO-OFDM at December and June solstices, respectively. The results show the SNR degradation effect on the BER performance for the OFDM-based VLC system. Both scenario II and scenario III at Antofagasta and Edinburgh are shown to allow the use of forward error correction (FEC) in both December and June solstice, although a significant improvement is shown to be achieved when the blue filter is used. The system performance

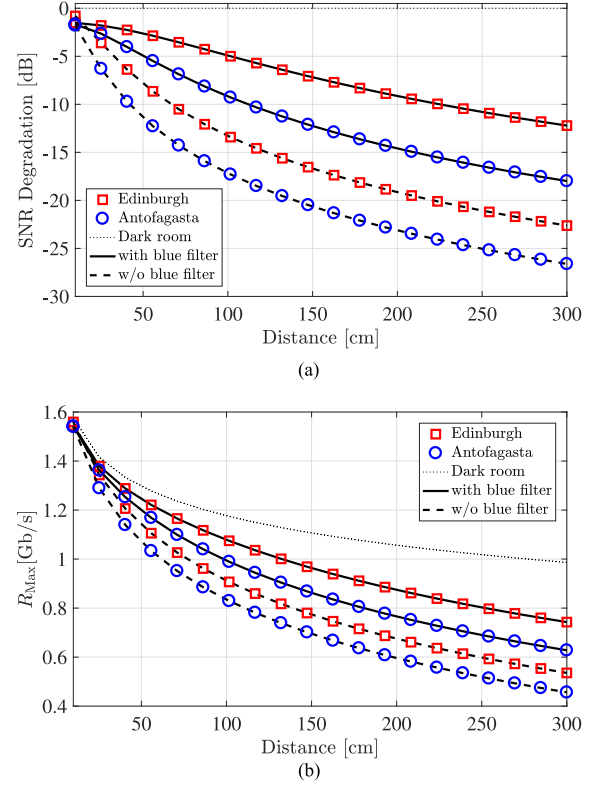


Fig. 6. System performance versus transmission distance d at the noon of the 20th of December 2016 for the three considered scenarios in Antofagasta and Edinburgh. (a) SNR and (b) Maximum theoretical limit on data rate.

is investigated as a function of the maximum theoretical limit to the data rate versus the time of the day in Fig. 4(e) and (f) for December and June solstices, respectively. The performance of Scenario II and the performance of Scenario III are compared to the benchmark performance recorded at 1.25 Gb/s of Scenario I for Antofagasta and Edinburgh. It is shown that the data rate degrades by 21.35% and by 15.49% at the noon of December solstice when the blue filter is not used in Antofagasta and Edinburgh, respectively. However, this degradation is reduced to 10% and 5.22% for Scenario II at Antofagasta and Edinburgh, respectively. This is equivalent to a significant 53.16% and 66.30% improvement that is achieved by placing a blue filter in front of the APD. A maximum theoretical limit to the data rate for June solstice under the solar irradiance is estimated at 1.03 Gb/s and 0.99 Gb/s for Scenario III at Antofagasta and Edinburgh, respectively and at 1.14 Gb/s and 1.13 Gb/s for Scenario II at Antofagasta and Edinburgh, respectively. A comparison of the maximum data rate performance at both Antofagasta and Edinburgh at noons of the last six months of 2016 is presented in Fig. 5(b). The variations in data rates are more noticeable for Edinburgh, where it increases to reach a maximum of 1.19 Gb/s for Scenario II and 1.06 Gb/s for Scenario III in December.

The SNR degradation and the maximum theoretical limit on the data rate are given in Fig. 6(a) and (b) as functions of the transmission distance. The results in Fig. 6 are presented for the three considered scenarios at Antofagasta and Edinburgh at noon of the 20th of December 2016. The SNR degrades as the transmission distance increases in all considered scenarios,

including the dark room scenario I, as expected. However, the SNR degradation for Scenario II and III are calculated with reference to the dark room in scenario I to highlight the solar irradiance effect in comparison with the benchmark Scenario I. It is shown that the SNR degradation reaches -26.61 dB and -22.63 dB when the blue filter is not used in Scenario III at a transmission distance of 3 meters at Antofagasta and Edinburgh, respectively. Although the SNR degradation appears to be high, the SNR gain of using the blue filter in Scenario II reaches 8.6 dB and 10.41 dB at a transmission distance of 3 meters for Antofagasta and Edinburgh, respectively. Similarly, the maximum theoretical limit on the data rate is shown to decrease as the transmission distance increases. The maximum theoretical limit on the data rate at a transmission distance of 3 meters for the dark room in Scenario I is 986.3 Mb/s. This is degraded by 53.74% for Antofagasta and 45.71% for Edinburgh in Scenario III. However, it is shown that the degradation is reduced to 36.33% and 24.7% in Antofagasta and Edinburgh when the blue filter is used in Scenario II. Despite the degradation in SNR, high-speed VLC can still be available at sufficiently long distances.

IV. EXPERIMENTAL STUDY

A. Experimental Set-Up

The measurements were conducted between 11:00–17:00 (local time) of the 6th and 9th of June 2016 under clear sky weather conditions demonstrated by very good visibility estimated above 21 km and a solar illuminance measured at 50350 lux. The measurements were carried at $55^{\circ}55'20.4''\text{N}$ $3^{\circ}10'23.3''\text{W}$ in Edinburgh, UK. The experimental setup is shown in Fig. 7(a)–(b). The system elements used in the experiment are the same components described in Section III-A. The OFDM modulation waveform is generated and processed off-line using MATLAB. The OFDM digital waveform is converted into an analog waveform using the arbitrary waveform generator Agilent 81180A, which sends the bipolar OFDM waveform to the micro-LED using a Bias-Tee ZFBT-4R2GW. The DC bias is selected after exhaustive tests at $V_{\text{DC}} = 4.1$ Volts to minimize the clipping distortion. The optical power of the micro-LED is 4.5 mW and the 3-dB bandwidth is 30 MHz, both measured at DC current $I_{\text{DC}} = 50$ mA. An aspheric collimation lens ACL 4532 is used to focus the light on the photoreceiver. Two Silicon APDs are used in this experiment (Hamamatsu, S8664-05k) and (Hamamatsu, S8664-50k), as shown in the top-right corner of Fig. 7(b). These APDs are referred to as ‘small’ APD and ‘large’ APD, respectively. The small APD has a smaller active area of 0.19 mm^2 and therefore, has a lower capacitance that leads to a higher 3-dB bandwidth of 680 MHz. The large APD has a larger active area of 19.6 mm^2 that leads to a higher capacitance and lower 3-dB bandwidth of 60 MHz.

The received signal at the APDs is filtered using a low pass electrical filter (Mini-circuits, SLP-100+) with a cut-off of 98 MHz for the large APD; and (Mini-circuits, SLP-250+) with a cut-off of 225 MHz for the small APD. Both filters are shown in Fig. 7(a). The system modulation bandwidth is used at 100 MHz and 250 MHz for the large and small APDs, re-

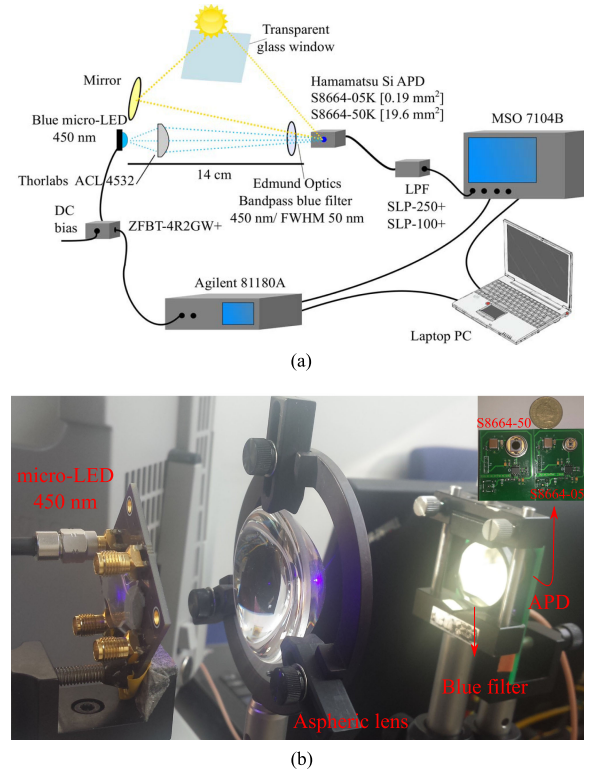


Fig. 7. The experimental set-up. (a) Schematic set-up of the experiment showing the optical system, arbitrary waveform function generator, oscilloscope, electrical and optical filters and Bias-T. (b) Photograph of the optical system showing the micro-LED, optical lenses system and the used APDs. In the top right corner (left): large APD s8664-50k; (right): small APD S8664-05k.

spectively. This is experimentally determined as the maximum bandwidth that allows for a SNR higher than 0 dB to be achieved. The electrical signal is then captured using an oscilloscope (Agilent, MSO7104B) and then processed using MATLAB. The overall distance between the micro-LED and the photodetector is 14 cm. The received optical power from the micro-LED would decrease at longer distances and consequently this would degrade the SNR because the SNR diminishes as the desired signal diminishes, but not because of noise due to sunlight. The distance is limited by the optical power of the micro-LED and it can be improved using more advanced collimation optics or using micro-LEDs with multiple pixels in a ganging mode [22]. The three scenarios described in Section III-A are considered in the experimental study. The SNR of the channel is first estimated and then the constellation sizes and the associated power of M -QAM symbols are adaptively allocated to each subcarrier based on the estimated SNR. The adaptive bit and energy loading algorithm avoids the use of low-frequency subcarriers, where the interference of ambient light can be strong. In addition, it avoids any other subcarrier, where the SNR is expected to result in a BER below the FEC target.

B. Results and Discussions

The measured solar irradiance is given in Fig. 8 for the wavelengths between 350 and 750 nm covering the visible spectrum and part of the infrared and ultraviolet spectra. Four cases are presented: direct sunlight; reflected sunlight from a mirror,

TABLE II
ACHIEVABLE SNR VALUES AND DATA RATES FOR THE SMALL AND LARGE APDs FOR THE THREE CONSIDERED SCENARIOS

	Dark room (Scenario I)		with blue filter (Scenario II)		w/o blue filter (Scenario III)	
	Large APD	Small APD	Large APD	Small APD	Large APD	Small APD
Average SNR [dB]	17.57	18.58	16.64	17.36	12.42	16.42
Data rate @ BER<3.8e-3 [Mb/s]	416.44	1139.26	396.71	1080	313.35	1015

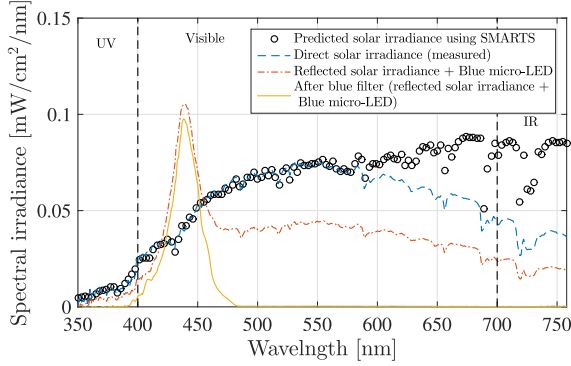


Fig. 8. The spectral distribution of the solar irradiance measured and predicted using SMARTS [20], [21] for Edinburgh (direct, reflected and filtered) in the presence and absence of the desired signal at 450 nm.

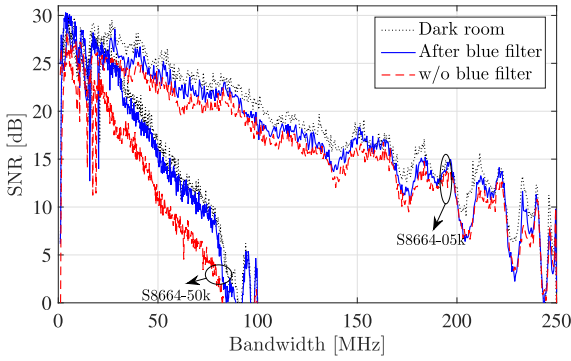


Fig. 9. Experimentally estimated SNR versus the system bandwidth when small and large APDs are used for the three considered scenarios.

reflected sunlight and blue micro-LED (Scenario III); and reflected sunlight and blue micro-LED with a blue optical filter (Scenario II). The experiment was conducted inside a building where the direct sunlight is passed through a transparent glass window before it is collected at the photoreceiver. It was practically infeasible to realize the experimental setup while the direct solar irradiance is always focused into the APD due to the varying solar position throughout the experiment duration. A mirror was used to work around this issue at the expense of reduced solar irradiance. This was shown to have little impact on the blue band below 450 nm as it is shown in Fig. 8. The experimentally measured direct solar irradiance is shown to be identical to the simulated solar irradiance below 580 nm. The mismatch at longer wavelengths is attributed to the high reflectance and less transmittance characteristics of heat mirrors glazing in the infrared band that aim to improve building heat insulation [34].

The experimentally estimated SNR is presented in Fig. 9 for the small and large APDs at all the considered scenarios. All the performance comparisons are presented with reference to the optimal dark room (Scenario I). It is shown that the performance of the VLC system degrades in the presence of

direct sunlight for both APDs. The degradation in the average SNR is estimated at 2.16 dB for the small APD and 5.15 dB for the large APD in Scenario III. The photocurrents generated by both signal and background noise generally increase as the detection area of the APD increases. However, an optical source with small emission area and an imaging lens are used in this experiment to focus the light into the APD. The focused light spot size at the APD can ideally be as small as the emission area of the micro-LED (0.01 mm²) [35]. Therefore, The signal photocurrent does not increase when the detection area becomes larger than the focused light spot at the APD. This validates the result that the SNR degradation is higher for the large APD, because it collects more background light. When the blue filter is used to restrict the unwanted irradiance, the degradation in the average SNR is reduced to 1.22 dB for the small APD and 0.93 dB for the large APD. Similar trends are presented in Table II for the achieved data rates. All the presented data rates are achieved below the FEC limit of 3.8×10^{-3} . The data rate decreases in the presence of solar irradiance. However, most of this reduction can be recovered using the blue filter. It is shown that a data rate of 1.015 Gb/s can be achieved under the presence of solar irradiance for the small APD in Scenario III. This is equivalent to a 10.4% reduction in data rate compared to Scenario I. This degradation can be reduced to 5.2% when the blue filter is used. A reduction of 24.75% in the data rates is witnessed in Scenario II for the large APD. This is improved to 4.73% when using the blue filter in Scenario II.

V. CONCLUSION

VLC system is feasible in the presence of solar irradiance. Worst-case scenarios are considered in this study to prove the concept that VLC systems can work under the influence of strong solar irradiance. Shot noise caused by sunlight reduces the data rate of VLC systems. However, optical bandpass blue filters can limit the degradation caused by solar irradiance. Data rates above 1 Gb/s were experimentally achieved in the presence of solar irradiance without optical filtering. Simulation results have shown that an improvement of at least 6.47 dB can be achieved for SNR using off-the-shelf blue filters.

Saturation is a major drawback for photodiodes in the presence of strong background noise. Automatic gain controller (AGC) can be used to reduce the likelihood of performance outage due to APD saturation. However, this is not considered in the current work and will be considered in future research. Bandpass optical filtering was considered as a technique to mitigate solar irradiance noise. However, the results of this study can be used to build upon and to develop new solar irradiance noise mitigation techniques. An interesting solution could be envisaged to use angle-diversity receiver with signal combining techniques. However, the details of such investigation is out the scope of this paper and will be considered in future research.

APPENDIX A SOLAR POSITION

Three coordinate systems are used to calculate the position of the Sun: ecliptic coordinates; equatorial coordinates; and horizontal coordinates. These coordinate systems can be illustrated on the celestial sphere shown in Fig. 10. The parameters corresponding to each coordinate system are mapped in Table III. The arbitrary coordinates in Fig. 10 is defined by Θ which is the angle between the principle and the projection of the Sun at the fundamental plane and by Ξ which is the angle between the Sun and the fundamental plane. Celestial coordinate systems can be converted into Cartesian coordinates using:

$$\begin{pmatrix} X \\ Y \\ Z \end{pmatrix} = \begin{pmatrix} \cos \Xi \cos \Theta \\ \cos \Xi \sin \Theta \\ \sin \Xi \end{pmatrix}. \quad (14)$$

The horizontal coordinate system is usually used for solar cell applications where the horizon of the observer is the fundamental plane. The solar position can be projected on a celestial sphere using two angles: altitude Al and azimuth Az . The Earth revolves around the Sun in an elliptic orbit in which a complete revolution takes a year, a motion of around 1° per day. This motion can be best described using the ecliptic coordinates where the principle is the position of the Sun during the spring equinox (the date of the year when the Earth's equator is aligned with the center of the Sun ecliptic). The angular ecliptic coordinates are the ecliptic longitude, λ and ecliptic latitude, β , which is given as $\beta \approx 0$ [18]. The ecliptic longitude can be given as [18]:

$$\lambda = q + 1.915^\circ \sin q + 0.020^\circ \sin 2q, \quad (15)$$

where q is the mean longitude given as [18]:

$$q = 280.459^\circ + 0.98564736^\circ D, \quad (16)$$

and g is the mean anomaly of the Sun, which accounts for the varying speeds of the Earth motion throughout the year. This is given as [18]:

$$g = 357.529^\circ + 0.98560028^\circ D, \quad (17)$$

where D is the time elapsed since the Greenwich noon of the 1st of January 2000.

The equatorial coordinate system is required as a translational stage when transforming the ecliptic coordinates into horizontal coordinates, as follows:

$$\begin{pmatrix} X_{\text{Equ}} \\ Y_{\text{Equ}} \\ Z_{\text{Equ}} \end{pmatrix} = \begin{pmatrix} 1 & 0 & 0 \\ 0 & \cos \epsilon & -\sin \epsilon \\ 0 & \sin \epsilon & \cos \epsilon \end{pmatrix} \begin{pmatrix} X_{\text{Ecl}} \\ Y_{\text{Ecl}} \\ Z_{\text{Ecl}} \end{pmatrix}, \quad (18)$$

where ϵ is the axial tilt between the equatorial plane and the ecliptic plane. The axial tilt is zero in March and September equinox and takes its maximum value of $\pm 23.429^\circ$ in June and December solstices (the days when the maximum tilt is experienced at the north and south hemisphere, respectively). The axial tilt is given as [18]:

$$\epsilon = 23.429^\circ - 0.00000036^\circ D. \quad (19)$$

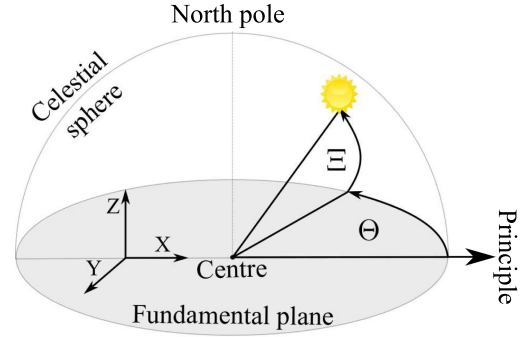


Fig. 10. An illustration of an arbitrary coordinate system on a celestial sphere.

TABLE III
COORDINATION SYSTEMS CORRESPONDING PARAMETERS

Arbitrary	Ecliptic	Equatorial	Horizontal
center	center of the Earth	center of the Earth	observer
north pole	north ecliptic pole	north celestial pole	zenith
fundamental plane	ecliptic	celestial equator	horizon
principle	March equinox	March equinox	geographic north pole
Θ	ecliptic longitude (λ)	right ascension (α)	azimuth (Az)
Ξ	ecliptic latitude (β)	declination (δ)	altitude (Al)
$\begin{pmatrix} X \\ Y \\ Z \end{pmatrix}$	$\begin{pmatrix} X_{\text{Ecl}} \\ Y_{\text{Ecl}} \\ Z_{\text{Ecl}} \end{pmatrix}$	$\begin{pmatrix} X_{\text{Equ}} \\ Y_{\text{Equ}} \\ Z_{\text{Equ}} \end{pmatrix}$	$\begin{pmatrix} X_{\text{Hor}} \\ Y_{\text{Hor}} \\ Z_{\text{Hor}} \end{pmatrix}$

The equatorial coordinates are given by the right ascension α which is the angle between the March equinox and the projection of the Sun on the Earth's equator and by the declination δ which is the angle between the Sun and the Earth equator. The Sun moves 15° of longitude per hour. The hour angle is defined as the angle between the projection of the Sun on the fundamental plane and the meridian given at longitude of 0° (an imaginary circle passing through the north and south poles and the zenith of an observer). The hour angle is given by:

$$h = \theta_L - \alpha, \quad (20)$$

where θ_L is the angle between the meridian and the March equinox. It can also be defined as the local mean sidereal time (LMST). A sidereal day is the time that the Earth takes to complete a 360° rotation on its own axis. It is slightly shorter than the solar day mainly due to the rotation of the Earth around the Sun. The LMST can be given as:

$$\theta_L = \text{GMST} \frac{15^\circ}{\text{hour}} + \lambda_0, \quad (21)$$

where λ_0 is the longitude of the observer and GMST is the Greenwich mean sidereal time (GMST), which is defined as the hour angle between the March equinox and the meridian at Greenwich. GMST is calculated as [18]:

$$\text{GMST} = 18.697374558\text{h} + 24.06570982441908\text{h}D, \quad (22)$$

where it is scaled to values between 0 and 24.

The principle of the coordinates can be transformed from the March equinox to the LMST using:

$$\begin{pmatrix} \cos \delta \cos h \\ \cos \delta \sin h \\ \sin \delta \end{pmatrix} = \begin{pmatrix} \cos \theta_L & \sin \theta_L & 0 \\ 3pt \sin \theta_L & -\cos \theta_L & 0 \\ 0 & 0 & 1 \end{pmatrix} \begin{pmatrix} X_{\text{Equ}} \\ Y_{\text{Equ}} \\ Z_{\text{Equ}} \end{pmatrix}, \quad (23)$$

In addition, the center of the coordinates can be transformed from the center of the Earth to the position of the observer using:

$$\begin{pmatrix} X'_{\text{Hor}} \\ Y'_{\text{Hor}} \\ Z'_{\text{Hor}} \end{pmatrix} = \begin{pmatrix} \sin \phi_0 & 0 & -\cos \phi_0 \\ 0 & 1 & 0 \\ \cos \phi_0 & 0 & \sin \phi_0 \end{pmatrix} \begin{pmatrix} \cos \delta \cos h \\ \cos \delta \sin h \\ \sin \delta \end{pmatrix} \quad (24)$$

Following the prior calculations, the directions of X'_{Hor} and Y'_{Hor} are directed towards south and west, respectively. The following can be applied to adjust the reference direction to north and east [18]:

$$\begin{pmatrix} X_{\text{Hor}} \\ Y_{\text{Hor}} \\ Z_{\text{Hor}} \end{pmatrix} = \begin{pmatrix} -1 & 0 & 0 \\ 0 & -1 & 0 \\ 0 & 0 & 1 \end{pmatrix} \begin{pmatrix} X'_{\text{Hor}} \\ Y'_{\text{Hor}} \\ Z'_{\text{Hor}} \end{pmatrix} \quad (25)$$

The horizontal coordinates can then be calculated using [18]:

$$\sin Al = \cos \phi_0 \cos \theta_L \cos \lambda_S + (\cos \phi_0 \sin \theta_L \cos \epsilon + \sin \phi_0 \sin \epsilon) \sin \lambda_S \quad (26)$$

$$\tan Az = \frac{\Gamma_1}{\Gamma_2 - \Gamma_3}, \quad (27)$$

where:

$$\Gamma_1 = -\sin \theta_L \cos \lambda_S + \cos \theta_L \cos \epsilon \sin \lambda_S, \quad (28)$$

$$\Gamma_2 = -\sin \phi_0 \cos \theta_L \cos \lambda_S, \quad (29)$$

$$\Gamma_3 = \sin \lambda_S (\sin \phi_0 \sin \theta_L \cos \epsilon - \cos \phi_0 \sin \epsilon), \quad (30)$$

REFERENCES

- [1] Cisco Visual Networking Index, "Global mobile data traffic forecast update, 2015-2020," CISCO, White Paper, Feb. 2016. [Online]. Available: <http://www.cisco.com/c/en/us/solutions/collateral/service-provider/visual-networking-index-vni/mobile-white-paper-c11-520862.pdf>
- [2] OFCOM report, "Award of the 2.3 and 3.4 GHz Spectrum Bands: Competition issues and auction regulations," OFCOM, Consultation, Jan. 2017. [Online]. Available: https://www.ofcom.gov.uk/data/assets/pdf_file/0026/93545/award-of-the-spectrum-bands-consultation.pdf
- [3] S. Dimitrov and H. Haas, *Principles of LED Light Communications: Towards Networked Li-Fi*. Cambridge, U.K.: Cambridge Univ. Press, 2015.
- [4] M. S. Islam *et al.*, "Towards 10 Gb/s orthogonal frequency division multiplexing-based visible light communication using a GaN violet micro-LED," *Photon. Res.*, vol. 5, no. 2, pp. A35–A43, Apr. 2017. [Online]. Available: <http://www.osapublishing.org/prj/abstract.cfm?URI=prj-5-2-A35>
- [5] D. Tsonev, S. Videv, and H. Haas, "Towards a 100 Gb/s visible light wireless access network," *Opt. Express*, vol. 23, no. 2, pp. 1627–1637, Jan. 2015. [Online]. Available: <http://www.opticsexpress.org/abstract.cfm?URI=oe-23-2-1627>
- [6] G. Povey, "Top 10 Li-Fi myths," Jun. 2012. [Online]. Available: <http://visiblelightcomm.com/top-10-li-fi-myths/>
- [7] M. S. Islam and H. Haas, "Modulation techniques for Li-Fi," *ZTE Commun.*, vol. 14, no. 2, pp. 29–40, Apr. 2016.
- [8] Y. H. Chung and S. B. Oh, "Efficient optical filtering for outdoor visible light communications in the presence of sunlight or artificial light," in *Proc. Int. Symp. Intell. Signal Process. Commun. Syst.*, Nov. 2013, pp. 749–752.
- [9] T. Hamza, M.-A. Khalighi, S. Bourennane, P. Léon, and J. Opderbecke, "Investigation of solar noise impact on the performance of underwater wireless optical communication links," *Opt. Express*, vol. 24, no. 22, pp. 25 832–25 845, Oct. 2016. [Online]. Available: <http://www.opticsexpress.org/abstract.cfm?URI=oe-24-22-25832>
- [10] M. Beshir, C. Michie, and I. Andonovic, "Evaluation of visible light communication system performance in the presence of sunlight irradiance," in *Proc. 2015 17th Int. Conf. Transp. Opt. Netw.*, Jul. 2015, pp. 1–4.
- [11] Y.-H. Kim and Y.-H. Chung, "Experimental outdoor visible light data communication system using differential decision threshold with optical and color filters," *Opt. Eng.*, vol. 54, pp. 1–3, 2015. [Online]. Available: <http://dx.doi.org/10.1117/1.OE.54.4.040501>
- [12] D. R. Kim, S. H. Yang, H. S. Kim, Y. H. Son, and S. K. Han, "Outdoor visible light communication for inter-vehicle communication using controller area network," in *Proc. 2012 4th Int. Conf. Commun. Electron.*, Aug. 2012, pp. 31–34.
- [13] ASTM, *Standard Tables for Reference Solar Spectral Irradiances: Direct Normal and Hemispherical on 37 Tilted Surface*, Standard ASTM-G173-03, 2014. [Online]. Available: <https://doi.org/10.1520/G0173-03R12>
- [14] M. Islam and H. Haas, "An investigation of the sunlight irradiance effect on visible light communications," in *Proc. 27th Int. Symp. Pers. Indoor Mobile Radio Commun.*, Montreal, QC, Canada, Oct. 8–13, 2017, pp. 1–6.
- [15] G. Cossu *et al.*, "Experimental demonstration of high speed underwater visible light communications," in *Proc. 2013 2nd Int. Workshop Opt. Wireless Commun.*, Oct. 2013, pp. 11–15.
- [16] ASTM, *Standard Solar Constant and Zero Air Mass Solar Spectral Irradiance Tables*, Standard ASTM-E490-00a, 2014. [Online]. Available: <https://doi.org/10.1520/E0490>
- [17] W. B. Stine and M. Geyer, *Power From the Sun*, 2001. [Online]. Available: <http://Powerfromthesun.net>
- [18] A. Smets, K. Jäger, O. Isabella, M. Zeman, and R. van Swaaij, *Solar Energy: The Physics and Engineering of Photovoltaic Conversion, Technologies and Systems*. Cambridge, U.K.: UIT Cambridge, 2016. [Online]. Available: <https://books.google.co.uk/books?id=vTkdgEACAAJ>
- [19] I. Reda and A. Andreas, "Solar position algorithm for solar radiation applications," *Sol. Energy*, vol. 76, no. 5, pp. 577–589, 2004.
- [20] C. A. Gueymard, "Parameterized transmittance model for direct beam and circumsolar spectral irradiance," *Sol. Energy*, vol. 71, no. 5, pp. 325–346, 2001.
- [21] C. Gueymard, *SMARTS2: A Simple Model of the Atmospheric Radiative Transfer of Sunshine: Algorithms and Performance Assessment*. Cocoa, FL, USA: Florida Solar Energy Center, 1995.
- [22] S. Rajbhandari *et al.*, "A review of gallium nitride LEDs for multi-gigabit-per-second visible light data communications," *Semicond. Sci. Technol.*, vol. 32, no. 2, 2017, Art. no. 023001. [Online]. Available: <http://stacks.iop.org/0268-1242/32/i=2/a=023001>
- [23] F. Xu, M. A. Khalighi, and S. Bourennane, "Impact of different noise sources on the performance of PIN- and APD-based FSO receivers," in *Proc. 11th Int. Conf. Telecommun.*, Jun. 2011, pp. 211–218.
- [24] R. Rondanelli, A. Molina, and M. Falvey, "The Atacama surface solar maximum," *Bull. Amer. Meteorol. Soc.*, vol. 96, no. 3, pp. 405–418, 2015. [Online]. Available: <https://doi.org/10.1175/BAMS-D-13-00175.1>
- [25] S. Dimitrov, S. Sinanovic, and H. Haas, "Signal shaping and modulation for optical wireless communication," *J. Lightw. Technol.*, vol. 30, no. 9, pp. 1319–1328, May 2012.
- [26] F. M. Davidson and X. Sun, "Gaussian approximation versus nearly exact performance analysis of optical communication systems with PPM signaling and APD receivers," *IEEE Trans. Commun.*, vol. 36, no. 11, pp. 1185–1192, Nov. 1988.
- [27] Hamamatsu Photonics K.K., "Characteristics and Use of SI-APD (avalanche photodiode)," May 2004. [Online]. Available: http://neutron.physics.ucsb.edu/docs/Characteristics_and_use_of_SI-APD.pdf
- [28] G. Keiser, *Optical Communications Essentials*. New York, NY, USA: McGraw-Hill, 2003.
- [29] J. M. Kahn and J. R. Barry, "Wireless infrared communications," *Proc. IEEE*, vol. 85, no. 2, pp. 265–298, Feb. 1997.
- [30] H. E. Levin, "A complete and optimal data allocation method for practical discrete multitone systems," in *Proc. IEEE Global Telecommun. Conf.*, San Antonio, TX, USA, Nov. 25–29, 2001, vol. 1, pp. 369–374.

- [31] C. Shannon, "A mathematical theory of communication," *Bell Syst. Tech. J.*, vol. 27, pp. 379–423 & 623–656, Jul./Oct. 1948.
- [32] S. Dimitrov and H. Haas, "Information rate of OFDM-based optical wireless communication systems with nonlinear distortion," *IEEE J. Lightw. Technol.*, vol. 31, no. 6, pp. 918–929, Mar. 2013.
- [33] F. Xiong, *Digital Modulation Techniques*, 2nd ed. Norwood, MA, USA: Artech House, 2006.
- [34] C. M. Lampert, "Heat mirror coatings for energy conserving windows," *Sol. Energy Mater.*, vol. 6, no. 1, pp. 1–41, 1981. [Online]. Available: <http://www.sciencedirect.com/science/article/pii/0165163381900472>
- [35] E. Diaz and M. Knobl, "Prototyping illumination systems with stock optical components," *Photonik Int.*, Fellbach, Germany, 2012.

Mohamed Sufyan Islam (S'07) received the M.Sc. degree (distinction) in communications engineering from Aleppo University, Aleppo, Syria, in 2013, and the M.Sc. degree (distinction) in signal processing and communications, from the University of Edinburgh, Edinburgh, U.K., in 2014. He is currently working toward the Ph.D. degree at the LiFi Research and Development Centre, University of Edinburgh. His research interests include optical OFDM, LiFi, and optical wireless communications. Among several scholarships he was awarded in 2013, he was the recipient of the Global Edinburgh Syrian Scholarship from Edinburgh University. He also received the 2014 IEEE communications chapter prize for the best master project.

Stefan Videv, biography not available at the time of publication.

Majid Safari (S'08–M'11) received the B.Sc. degree in electrical and computer engineering from the University of Tehran, Tehran, Iran, in 2003, the M.Sc. degree in electrical engineering from Sharif University of Technology, Tehran, Iran, in 2005, and the Ph.D. degree in electrical and computer engineering from the University of Waterloo, Waterloo, ON, Canada, in 2011.

He is currently an Assistant Professor with the Institute for Digital Communications, University of Edinburgh, Edinburgh, U.K. Before joining Edinburgh in 2013, he was a postdoctoral fellow with McMaster University, Hamilton, ON, Canada. His main research interest is the application of information theory and signal processing in optical communications including fiber-optic communication, free-space optical communication, visible light communication, and quantum communication.

Dr. Safari is currently an Associate Editor for the IEEE COMMUNICATION LETTERS and was the TPC co-chair for the 4th International Workshop on Optical Wireless Communication in 2015.

Enyuan Xie received the Ph.D. degree in physics from the University of Strathclyde, Glasgow, U.K., in 2013. Since then, he has been with the Institute of Photonics, University of Strathclyde, Glasgow, U.K., as a research fellow, becoming involved in the fabrication, characterization, and application of GaN-based micro-LED arrays.

Jonathan J. D. McKendry received the M.S. degree in electronics and electrical engineering from the University of Glasgow, Glasgow, U.K., in 2006, and the Ph.D. degree from the University of Strathclyde, Glasgow, U.K., in 2011. In 2007, he joined the Institute of Photonics as a Ph.D. student where the focus of his Ph.D. was on the application of AlInGaN-based micro-LEDs for time-resolved fluorescence lifetime measurements and optical communications. He currently works as a Research Associate with the Institute of Photonics, University of Strathclyde, Glasgow, U.K., primarily on the subject of LED-based visible light communications. To date, he has authored or co-authored more than 30 peer-reviewed journal articles and 30 conference submissions.

Erdan Gu received the Ph.D. degree in thin film physics from Aberdeen University, U.K., in 1992. Afterward, he was a Research Fellow with the Cavendish Laboratory, Cambridge University, Cambridge, U.K. In 1997, he joined the Thin Film Group, Oxford Instruments plc, U.K. as a Senior Research Scientist working on superconducting photonic devices. Since July 2002, he has been with the Institute of Photonics, University of Strathclyde, Glasgow, U.K., where he is an Associate Director and a Research Team Leader. In the Institute of Photonics, he is working and playing a leading role in a range of research projects on photonic materials and devices, micro/nano optoelectronics, diamond photonics, and optoelectronic devices for visible light communications.

Martin D. Dawson (M'85–SM'98–F'09) is a physicist known for his work on lasers and compound semiconductors. He is the Director of Research with the Institute of Photonics, University of Strathclyde, Glasgow, U.K., which he helped establish 20 years ago, and he was also appointed Inaugural Head of the Fraunhofer Centre for Applied Photonics in October 2012. He has more than 30 years' experience of applied research gained in academia and industry in the U.K. and USA, and he has been involved in the formation and technical development of a number of spin-out businesses, most recently including mLED Ltd. He holds an EPSRC Programme Grant on visible light communications and gave a Rank Prize Lecture in 2014 on applied research in photonics. He was the recipient of the 2016 Gabor Medal and Prize by the Institute of Physics and the 2016 Aron Kessel Award by the IEEE Photonics Society.

Harald Haas (S'98–AM'00–M'03–SM'17–F'18) received the Ph.D. degree from the University of Edinburgh, Edinburgh, U.K., in 2001. He is currently the Chair of Mobile Communications, University of Edinburgh, and the Founder and Chief Scientific Officer of pureLiFi Ltd. pureLiFi Ltd has more than 50 employees and has operations in the USA and Singapore. He is also the Director of the LiFi Research and Development Center, University of Edinburgh. His main research interests include optical wireless communications, hybrid optical wireless and RF communications, spatial modulation, and interference coordination in wireless networks. He first introduced and coined spatial modulation and LiFi. LiFi was listed among the 50 best inventions in TIME Magazine 2011. He was an invited speaker at TED Global 2011, and his talk: "Wireless Data from Every Light Bulb" has been watched online more than 2.5 million times. He gave a second TED Global lecture in 2015 on the use of solar cells as LiFi data detectors and energy harvesters. This has been viewed online more than 2.0 million times. He holds 43 patents and has more than 30 pending patent applications. He has published more than 400 conference and journal papers including a paper in *Science*. His Google Scholar h-index is 67, and his works have been cited more than 19,000 times. He was on the Thomson Reuters list of highly cited scientists, 2017. He co-authors a book entitled: "*Principles of LED Light Communications Towards Networked Li-Fi*" (Cambridge University Press, Cambridge, U.K., 2015).

Prof. Haas is an editor for the IEEE TRANSACTIONS ON COMMUNICATIONS and the IEEE JOURNAL OF LIGHTWAVE TECHNOLOGY. He was the co-recipient of the recent Best Paper Awards at VTC-Fall, 2013, VTC-Spring 2015, ICC 2016, and ICC 2017. He was the co-recipient of the EURASIP Best Paper Award for the *Journal on Wireless Communications and Networking* in 2015 and co-recipient of the Jack Neubauer Memorial Award of the IEEE Vehicular Technology Society. He is the recipient of the Tam Dalyell Prize 2013 awarded by the University of Edinburgh for excellence in engaging the public with science. In 2016, he was the recipient of the Outstanding Achievement Award from the International Solid State Lighting Alliance, which was awarded to him by Prof. Shuji Nakamura. He has delivered 50 keynote talks at international conferences and workshops. In 2012, he was the recipient of the prestigious Established Career Fellowship from the Engineering and Physical Sciences Research Council within information and communications technology in the U.K. In 2014, he was selected by EPSRC as one of ten recognising inspirational scientists and engineers (RISE) Leaders in the U.K. He was elected a Fellow of the Royal Society of Edinburgh in 2017.